



Magnetic and microstructural properties of thin film Fe-Sb obtained by thermal evaporation of nanostructured milled powder

Ali Hafs^{1,2} · Toufik Hafs³ · Djamel Berdjane⁴ · Amel Bendjama⁴ · Nesrine Hasnaoui²

Received: 7 April 2024 / Accepted: 12 June 2024 / Published online: 4 July 2024
© The Author(s), under exclusive licence to Springer-Verlag London Ltd., part of Springer Nature 2024

Abstract

Nanostructured Fe₉₀Sb₁₀ (wt.%) alloys were synthesized via mechanical alloying of pure iron and antimony powders in a high-energy planetary ball mill. The milling duration was carefully optimized to achieve a nanostructured mixture and to form a supersaturated solid solution of (bcc) α -Fe(Sb). Subsequently, the powder mixture was utilized to deposit (bcc) α -Fe(Sb) onto a glass substrate. The fabrication of our films was carried out through thermal evaporation (physical vapor deposition) under a vacuum of 2.1×10^{-5} mbar, utilizing an electrically heated tungsten boat. The supersaturated solid solution (bcc) α -Fe(Sb) powder obtained via mechanical alloying was employed as the source material for deposition. In this study, we investigate the influence of milling time and film thickness on the structural, microstructural, and magnetic properties of Fe₉₀Sb₁₀ (wt.%) powders and thin films. Structural, microstructural, and magnetic analyses of the milled powders and thin films were conducted using X-ray diffraction (XRD), scanning electron microscopy (SEM), and vibrating sample magnetometry (VSM).

Keywords α -Fe(Sb) solid solution · Thin film · Structural · Microstructure · XRD · VSM

1 Introduction

In recent years, the field of nanomaterials and nanotechnologies has emerged as one of the most captivating and dynamic domains of scientific inquiry, captivating the minds of researchers and innovators across the globe [1–5]. Its appeal is rooted in the vast potential it holds, spanning both the fundamental principles of science and the practical applications that can transform industries and technologies [6, 7]. Among the diverse array of nanomaterials that have sparked tremendous interest and exploration, ferromagnetic thin films stand out as a category of paramount significance. From a technological perspective, these thin films have found their place at the intersection of scientific ingenuity

and practical utility, offering a myriad of applications that extend far beyond the conventional boundaries of materials science [8, 9].

At the heart of this burgeoning field is a profound appreciation for the potential that nanoscale materials and technologies bring to the table. The ability to engineer, manipulate, and control matter at the atomic and molecular level has unlocked an astonishing realm of possibilities. It enables the creation of materials with finely tuned properties and exceptional functionalities, serving as a bridge between theoretical knowledge and real-world applications. Within this transformative landscape, ferromagnetic thin films emerge as a remarkable subset, possessing the power to reshape how we interact with and harness magnetic properties [10].

From a technological standpoint, ferromagnetic thin films are not mere curiosities but rather invaluable tools with a diverse range of applications. They hold the potential to serve as the foundation for magnetic recording media, breathing life into data storage technologies that underpin our modern digital world. Whether it is the magnetic hard drives storing vast troves of information or the delicate magnetic heads that read and write data with astonishing precision, ferromagnetic thin films quietly underpin these systems, exemplifying their indispensable role in our daily lives [11, 12].

✉ Ali Hafs
hafs-ali@univ-eltarf.dz

¹ Department of Physics, University of Chadli Bendjedid, P. Box 73, 36000 El Tarf, Algeria

² LEREC Laboratory, Department of Physics, University of Badji Mokhtar, P. Box 12, 23000 Annaba, Algeria

³ LERICA Laboratory, Department of Electronics, University of Badji Mokhtar, P. Box 12, 23000 Annaba, Algeria

⁴ Research Center in Industrial Technologies (CRTI), P. O. Box 64, 16014 Cheraga, Algiers, Algeria

However, the significance of ferromagnetic thin films extends well beyond the realm of data storage. Their influence reaches into other corners of the scientific and technological landscape, illuminating new pathways for innovation. These materials can be integrated into sensor technologies, enabling the development of highly sensitive detectors for various physical phenomena. They offer potential solutions for enhancing the efficiency of energy conversion and storage systems, which have become paramount in addressing global challenges such as climate change. Moreover, they hold promise in the development of spintronics, a burgeoning field that explores the utilization of electron spin as a fundamental unit of information, thus opening new vistas in computing and electronics [13].

In the grand tapestry of nanomaterials and nanotechnologies, ferromagnetic thin films not only represent a fascinating subject of study but also a testament to the transformative power of scientific discovery. The fusion of fundamental insights with practical applications serves as the cornerstone of progress in the twenty-first century. As we embark on this journey of exploration into the world of ferromagnetic thin films, we find ourselves at the nexus of scientific curiosity and technological innovation [14, 15].

The (bcc) α -Fe(Sb) solid solution thin films are deposited onto glass substrates via vacuum thermal evaporation, with thicknesses varying across different samples. These thin films are derived from α -Fe(Sb) powders obtained after a specified duration of grinding. Our study aims to investigate the impact of thickness on the structural and magnetic properties of thin films composed of (bcc) α -Fe(Sb) solid solution. Through systematic variation of film thickness, we aim to elucidate how changes in thickness influence the structural and magnetic characteristics of the (bcc) α -Fe(Sb) solid solution thin films. This research endeavor is crucial for advancing our understanding of the behavior of thin films in various applications, such as magnetic recording, sensors, and spintronics.

2 Experimental

2.1 Synthesis of Fe–10Sb (wt.%) alloy particles

The synthesis of Fe–10Sb (wt.%) alloy particles was conducted through mechanical alloying, a widely used method for producing alloy powders with controlled composition and microstructure. Our starting materials comprised commercially available Fe (Alfa-Aesar, 99.9%, < 10 μ m) and Sb (Alfa-Aesar, 99.8%, < 40 μ m) powders.

The mechanical alloying process was carried out using a planetary RETSCH PM 400 ball mill. The milling conditions were carefully optimized to ensure the desired alloy composition and microstructure. The mill operated at a

rotational speed of 350 rpm, and a ball-to-powder weight ratio of 15:1 was maintained throughout the milling process.

To prevent oxidation of the powders during milling, the experiments were conducted under a controlled argon atmosphere. This protective atmosphere shielded the powders from atmospheric oxygen, ensuring the integrity of the alloy composition. Additionally, the milling process involved intermittent breaks, with each milling session lasting for 1 h followed by a 30-min rest period.

Several effective milling durations were investigated to understand the evolution of the alloy microstructure and composition. The selected durations ranged from 2 to 36 h, providing insight into the kinetics of the mechanical alloying process and the formation of the Fe–Sb alloy phases.

2.2 Deposition of solid solution (bcc) α -Fe(Sb) powder film

The deposition of solid solution (bcc) α -Fe(Sb) powder film was achieved through a thermal evaporation process. Initially, the α -Fe(Sb) powder, obtained through mechanical alloying, was loaded into a tungsten boat within a vacuum chamber. The chamber was evacuated to a pressure of 2.1×10^{-5} mbar to create a high-vacuum environment conducive to film deposition.

The thermal evaporation process was conducted using resistive heating. An MECA 2000 evaporator was employed for this purpose. The distance between the substrate, in this case, thoroughly cleaned Corning glass substrates, and the source (the loaded tungsten boat) was optimized to 50 mm to ensure uniform deposition.

During the deposition process, the α -Fe(Sb) powder in the tungsten boat was heated, causing it to sublime and form a vapor. This vapor then condensed onto the surface of the glass substrates, resulting in the deposition of a thin film of the α -Fe(Sb) solid solution. It is important to note that the film deposition was carried out at room temperature, without any additional heating applied to the substrates.

This deposition method offers precise control over the thickness and composition of the deposited films and enables uniform coverage over large substrate areas. Additionally, deposition at room temperature eliminates the risk of substrate deformation or thermal damage, making it suitable for delicate substrates like glass.

2.3 Characterization of milled powders and thin films

The structural and magnetic properties of the milled powders at various milling times and thin films at different thicknesses were meticulously characterized utilizing a suite of advanced techniques. X-ray diffraction (XRD) analysis was conducted using a state-of-the-art Bruker D8 Advance Eco

X-ray diffractometer equipped with a copper anticathode Cu-K α radiation operating at 40 kV and 40 mA. Employing a (θ – 2θ) Bragg–Brentano geometry and a wavelength of $\lambda = 1.541874$ Å, the experiments were carried out at an ambient temperature of 25 °C. The obtained diffractograms were refined using the highly sophisticated Rietveld method implemented in the specialized MAUD software (version 2.22), enabling precise determination of the crystalline phases and structural properties of both the powders and thin films [16].

In parallel, scanning electron microscopy (SEM) was employed using the Quantum 250—FEI electron microscope to conduct microstructural characterization and morphology analysis of the powder mixtures obtained at varying grinding durations and thin films at different thicknesses. SEM imaging provided invaluable insights into the surface morphology, particle size distribution, and overall uniformity of the synthesized samples, facilitating a deeper understanding of their microstructural features.

Furthermore, magnetic assessments were carried out using a highly sensitive MicroSense V7 model vibrating sample magnetometer (VSM) operating at room temperature. This advanced magnetometer allowed for the examination of hysteresis cycles, providing crucial information on magnetization saturation (M_s), coercivity (H_C), and remanent magnetization (M_r) based on the applied magnetic field. By analyzing these parameters, we gained significant insights into the magnetic behavior and performance of both the synthesized powders and thin films.

3 Results and discussion

3.1 Fe–10Sb (wt.%) milled powders

In Fig. 1a, X-ray diffraction (XRD) patterns for Fe–10Sb (wt.%) powder mixtures are presented, depicting the evolution of structural changes after mechanical alloying (MA) for varying durations at room temperature. Initially, the XRD peaks correspond to the pure iron and antimony components of the powder mixture (labeled as 0 h in Fig. 1a). For iron, reflections along the planes (110), (200), (211), (220), and (310) indicate a cubic structure (CC), while antimony exhibits reflections along the planes (012), (104), (040), and (116), indicative of a rhombohedral structure.

After 12 h of milling, a notable transformation is observed: the complete disappearance of antimony peaks, coupled with a subtle shift in the iron-related peaks towards smaller angles (as shown in Fig. 1b). This disappearance suggests the dissolution of antimony atoms into the iron lattice, leading to the formation of a bcc solid solution denoted as α -Fe(Sb). The slight angular shift in the iron peaks is attributed to the development of this α -Fe(Sb) solid solution

and the introduction of first-order internal stress during milling.

This first-order angular stress, operating at a macroscopic level, induces changes in the lattice parameter, thereby causing the observed angular shift in the XRD peaks [17–19]. This observation underscores the intricate structural alterations occurring during the mechanical alloying process, shedding light on the formation mechanisms of α -Fe(Sb) solid solutions and the role of milling-induced stresses in their development.

In Fig. 2, the evolution of the crystallite size ($\langle D \rangle$, nm) and microstrain ($\langle \sigma^2 \rangle^{1/2}$) with respect to the milling duration is depicted. Upon examining the graph, a noticeable trend emerges: as the milling time increases from 0 to 36 h, there is a consistent reduction in the average crystallite size ($\langle D \rangle$) from 59.95 to 18.16 nm. Concurrently, the microstrain ($\langle \sigma^2 \rangle^{1/2}$) experiences a corresponding increase from 0.076 to 0.19%.

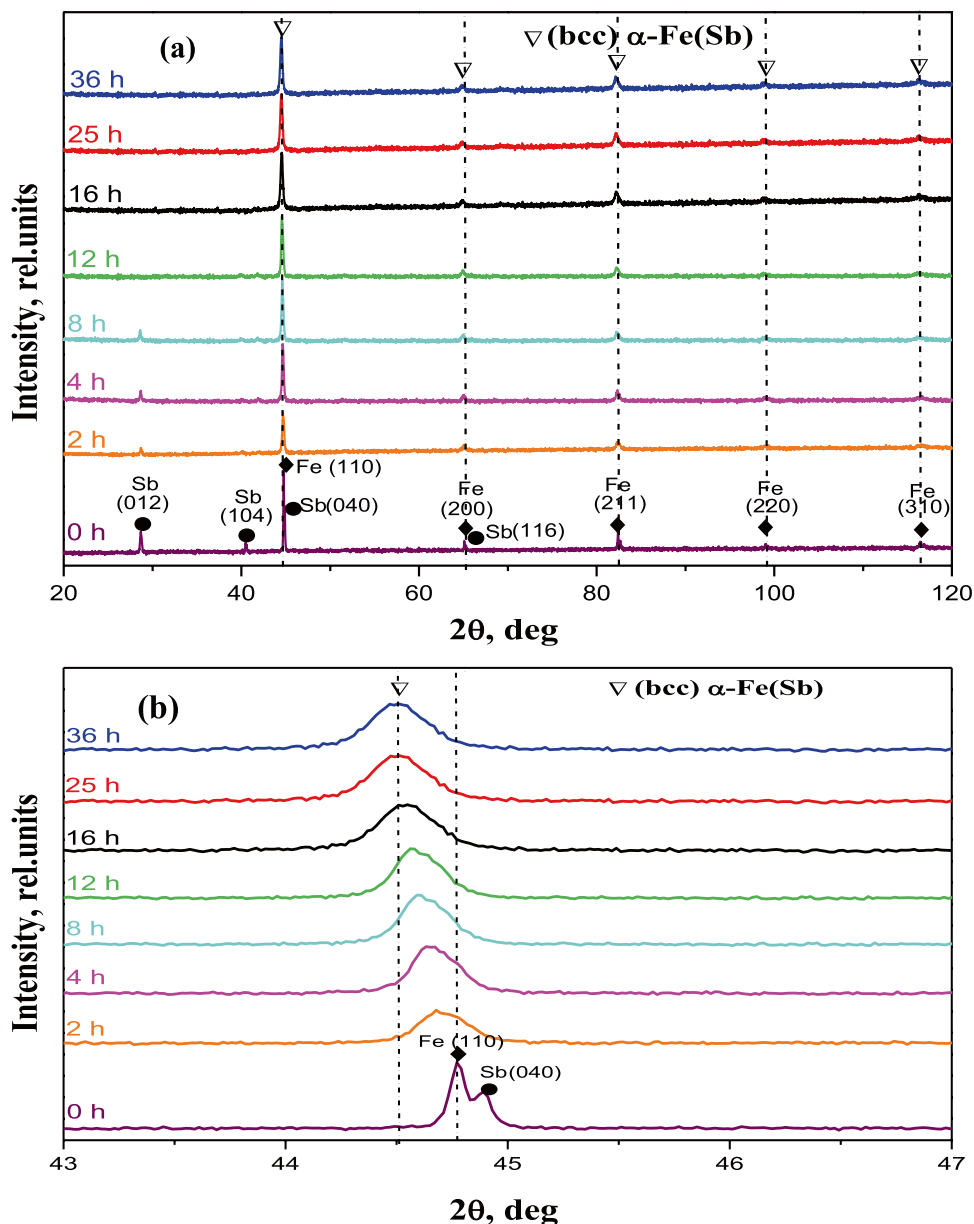
This observed decrease in $\langle D \rangle$ and the simultaneous rise in $\langle \sigma^2 \rangle^{1/2}$ can be attributed to the progressive hardening of the FeSb powders during milling. As the milling duration extends, the powders undergo increased deformation and fragmentation, leading to a refinement in the crystallite size. The enhanced hardness of the powders promotes more efficient grain fragmentation processes, resulting in the formation of smaller crystallites [20].

Overall, the findings from Fig. 2 highlight the dynamic nature of the mechanical alloying process and its profound impact on the structural properties of the FeSb powders. The observed trends underscore the effectiveness of milling in inducing structural modifications and refining the microstructure of the alloy, thereby contributing to the desired properties and performance of the synthesized material.

With the progression of milling times, there are noticeable alterations in the morphological structure of the macroscopic powders, as evidenced by the SEM micrographs in Fig. 3. In Fig. 3, SEM images display the particles of Fe₉₀Sb₁₀ powders after undergoing mechanical alloying for durations of 25 h and 36 h.

For the 25-h milling duration, as depicted in Fig. 3a, a noticeable transformation occurs in which the ground particles become smaller. Fine particles, approximately 5 μ m in size, emerge, exhibiting a relatively uniform appearance a hallmark of a delicate equilibrium between fracture and welding phenomena. During this stage, the bonding forces between the powder particles strengthen as the grain size reduces. Deformations are no longer easily achievable as they demand a substantial force for fracturing the particles. It becomes evident that the grain size decreases over the milling time, which is attributed to the interplay of fracture and welding processes resulting from the collisions between the powder, milling balls, and the inner wall of the container. At the 36-h mark of milling (as shown in Fig. 3b),

Fig. 1 **a** X-ray diffraction patterns of the $\text{Fe}_{90}\text{Sb}_{10}$ powders milled for different milling times. **b** Deconvolution of the most intense peak for different milling time



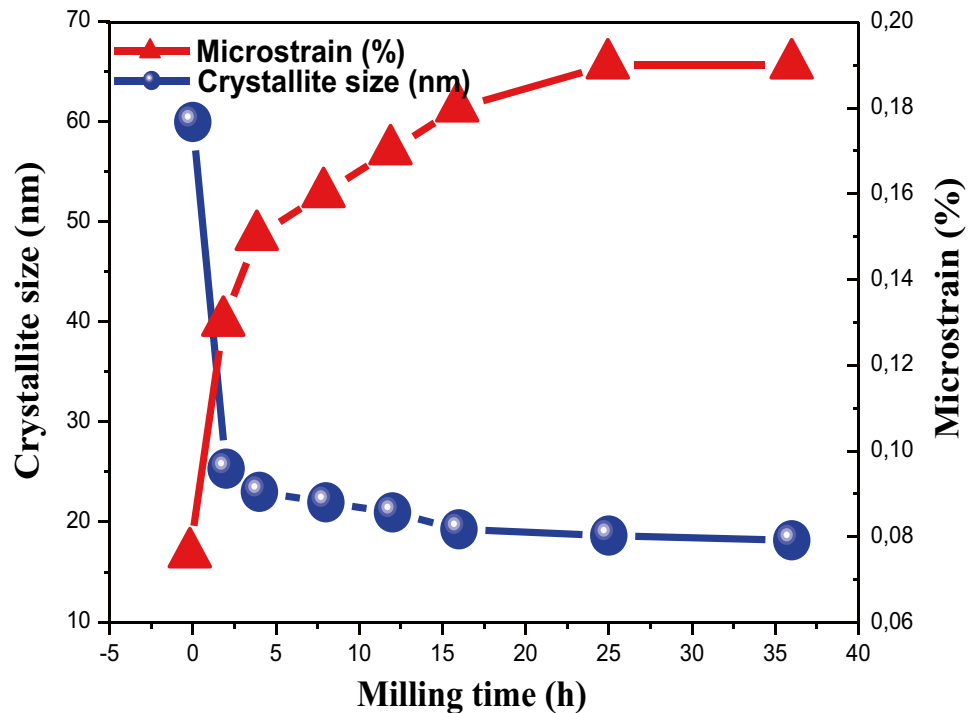
the observation reveals the presence of large agglomerates comprising exceedingly fine particles. These particles demonstrate a further refinement, becoming even finer and smaller with increased milling duration [21]. These findings indicate that after 36 h of milling, we obtain significantly smaller agglomerates compared to the preceding times, with the individual particles displaying greater homogeneity. It is noteworthy that, at this stage, the fracture process takes precedence in the mechanosynthesis, leading to a notable reduction in particle size.

The findings from the energy-dispersive X-ray (EDX) analysis conducted on $\text{Fe}_{90}\text{Sb}_{10}$ powders after both 25 and 36 h of grinding, as illustrated in Fig. 3c and d, serve as a robust confirmation of the anticipated elemental composition.

Specifically, the presence of iron (Fe) and antimony (Sb) aligns precisely with their nominal composition, substantiating the integrity of the material's chemical makeup. This validation not only underscores the accuracy of the material's composition but also lays a solid foundation for subsequent studies or applications within the field.

Of particular significance is the absence of any additional peaks in the EDX spectra, indicating the non-detection of chromium (Cr) contamination stemming from the milling elements (balls and jars). Moreover, the absence of oxygen (O_2) from the milling environment further reinforces the purity of the sample. Such meticulous analysis and confirmation of elemental composition are essential for ensuring the reliability and reproducibility of experimental results,

Fig. 2 Evolution of the average crystallite size, $\langle D \rangle$ (nm), and mean internal strain $\langle \sigma^2 \rangle^{1/2}$ (%), of $\text{Fe}_{90}\text{Sb}_{10}$ powders versus milling time



particularly in research endeavors aimed at elucidating the properties and behavior of materials under various conditions. Consequently, these results instill confidence in the suitability of the $\text{Fe}_{90}\text{Sb}_{10}$ powders for further investigations, whether in fundamental scientific inquiries or practical applications in industrial or technological domains.

The observed sigmoid-shaped hysteresis loops in Fig. 4, characteristic of nanostructured magnetically soft materials with small magnetic domains (as indicated in the inset of Fig. 4), are notable. This shape is indicative of the presence of structural distortions within the grains, contributing to the material's behavior. These distortions result in low hysteresis losses, a highly desired characteristic in soft magnetic materials. Such low losses imply enhanced efficiency in energy conversion, making these materials promising for various technological applications in areas like power electronics, sensors, and magnetic storage devices. This signifies that the material exhibits properties suitable for specific technological advancements, especially in optimizing energy use and magnetic storage capabilities [19].

3.2 Solid solution (bcc) α -Fe(Sb) powder thin films

Figure 5 illustrates the X-ray diffraction patterns of the solid solution of (bcc) α -Fe(Sb) powder thin films obtained by evaporation onto a glass substrate with varying thicknesses. The selected powder, subjected to 25 h of grinding, was used in the process. For the sample with a thickness of 16 nm, a single peak emerged, displaying a relatively low intensity. This peak, positioned at an angle of $2\theta = 44.65^\circ$, was

assigned to the body-centered cubic (bcc) α -Fe(Sb) (110) solid solution. Upon increasing the thickness to 25 nm, the emergence of the (110) peak is accompanied by the appearance of a slightly intensified peak corresponding to the (200) plane of the α -Fe(Sb) phase. For the thicker films with thicknesses of $t = 60$ nm and $t = 90$ nm, besides the presence of the (111) peak, additional peaks at $2\theta = 65.10^\circ$ and 82.31° appeared. These peaks have been identified as corresponding to the (200) and (211) planes of the α -Fe(Sb) phase, respectively. The distinct peaks observed in the X-ray diffraction patterns as the film thickness increases suggest notable variations in the crystallographic structure. These peaks, representing specific planes, serve as indicators of the crystalline orientation within the $\text{Fe}_{90}\text{Sb}_{10}$ films. The prominence of certain crystallographic planes, such as (110), underscores the evolving nature of the α -Fe(Sb) phase in response to changes in thickness. Understanding the structural characteristics of these films is of paramount importance. The arrangement of atoms in the crystal lattice, as revealed by the presence and intensity of these peaks, provides crucial insights. This information can guide further investigations into the properties and applications of $\text{Fe}_{90}\text{Sb}_{10}$ films across different thicknesses. The evolving nature of the α -Fe(Sb) phase suggests a dynamic relationship between film thickness and crystallographic behavior. This relationship may be influenced by factors such as strain, defects, or variations in the deposition process. By unraveling these connections, researchers can gain a deeper understanding of the material's behavior and tailor its properties for specific applications. The significance of this information extends

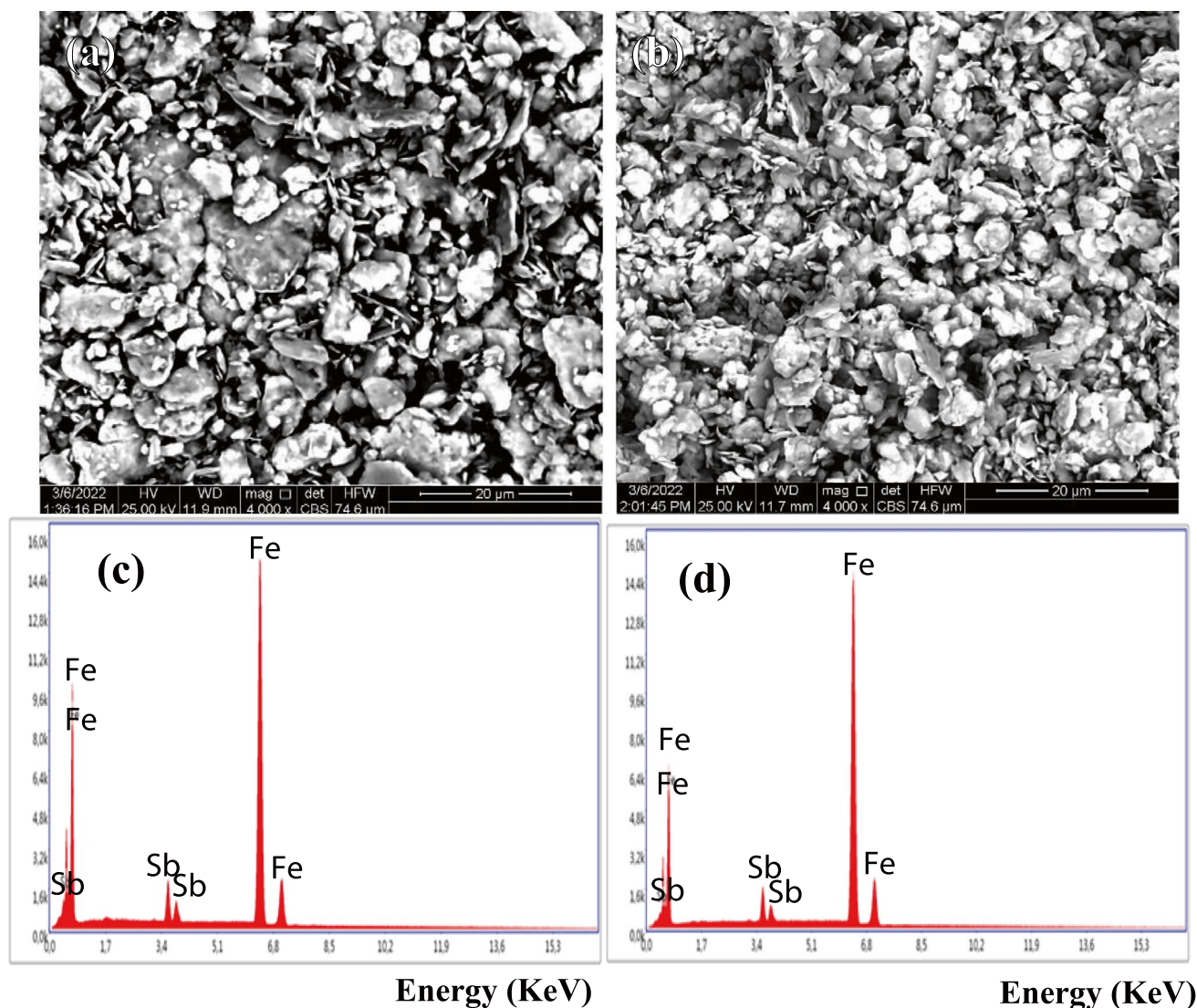


Fig. 3 SEM images showing the shape evolution of the $\text{Fe}_{90}\text{Sb}_{10}$ powder mixtures at different milling times **a** 25 h and **b** 36 h, respectively, and EDX plots of the $\text{Fe}_{90}\text{Sb}_{10}$ powder mixtures for various milling times **c** 25 h and **d** 36 h

to practical implications. Tailoring the film thickness could serve as a strategic approach for engineering desired properties in $\text{Fe}_{90}\text{Sb}_{10}$ films. Whether for applications in sensors, electronic devices, or other technological advancements, a comprehensive understanding of the structural characteristics is essential.

The lattice parameter is a crucial factor as it offers insights into the state of stresses imposed on the thin layer. The changes in lattice parameters across all samples, influenced by thickness, were identified through the Rietveld refinement of the X-ray diffraction spectrum, as illustrated in Fig. 6.

In Fig. 6, it is illustrating that the lattice parameter a (nm) monotonously decreases with the augmentation of thickness. Specifically, the value of a (nm) ranges from

(0.2859 ± 0.0001) nm for 16 nm to (0.2841 ± 0.0001) nm for 90 nm. Additionally, it is noteworthy that these values are below the bulk value, which equals 0.2866 nm [22]. Lamrani et al. [23] have previously reported a similar trend in the behavior of “ a ” (Å) concerning film thickness. This study utilized thermal evaporation for an $\text{Ni}_{80}\text{Fe}_{20}$ alloy, considering thicknesses of 16, 25, 60, and 90 nm.

The observed monotonic decrease in the lattice parameter with increasing thickness suggests a systematic trend in the crystal structure. The reduction in “ a ” indicates a possible compression or contraction of the lattice as the film thickness grows. This phenomenon could be influenced by factors such as strain, defects, or variations in the growth conditions during film deposition. Furthermore, the observed values being below the bulk value suggests that the thin films may

Fig. 4 Hysteresis loops (M–H curves) at room temperature of the Fe₉₀Sb₁₀ powders milled for a 0, 2, 4, 8, 12, 16, 25, and 36 h

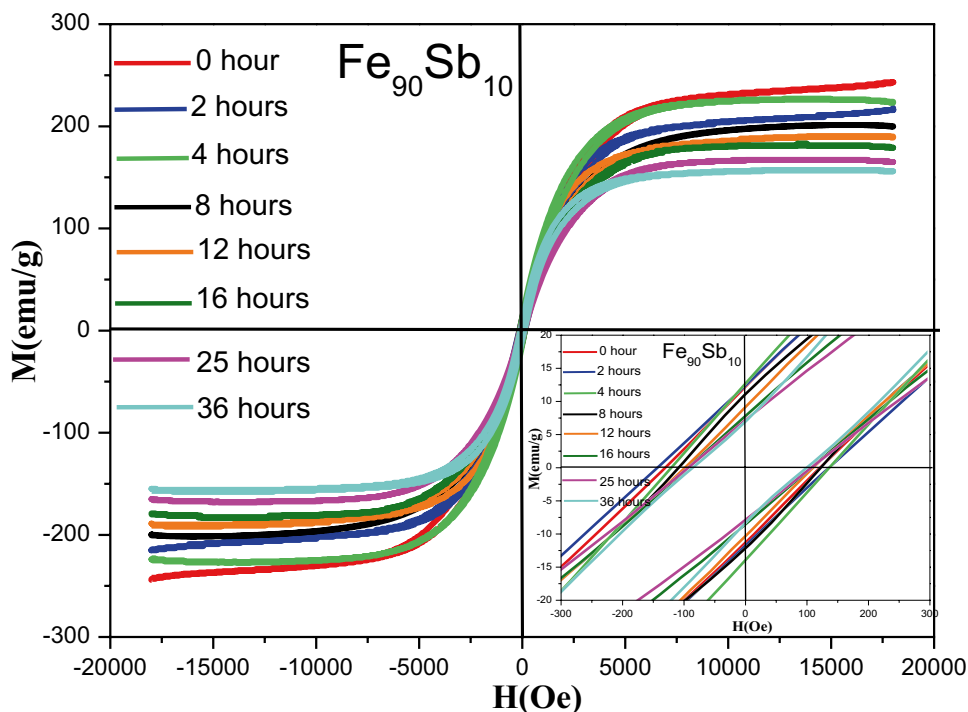
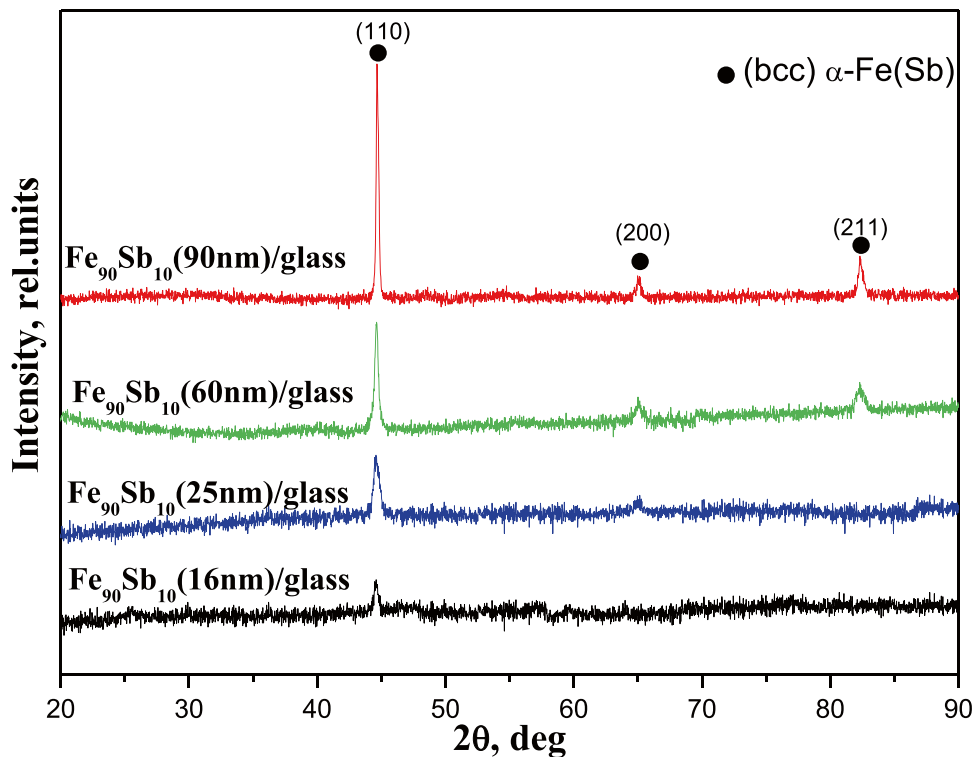


Fig. 5 X-ray diffraction spectra of Fe₉₀Sb₁₀ films for various thicknesses



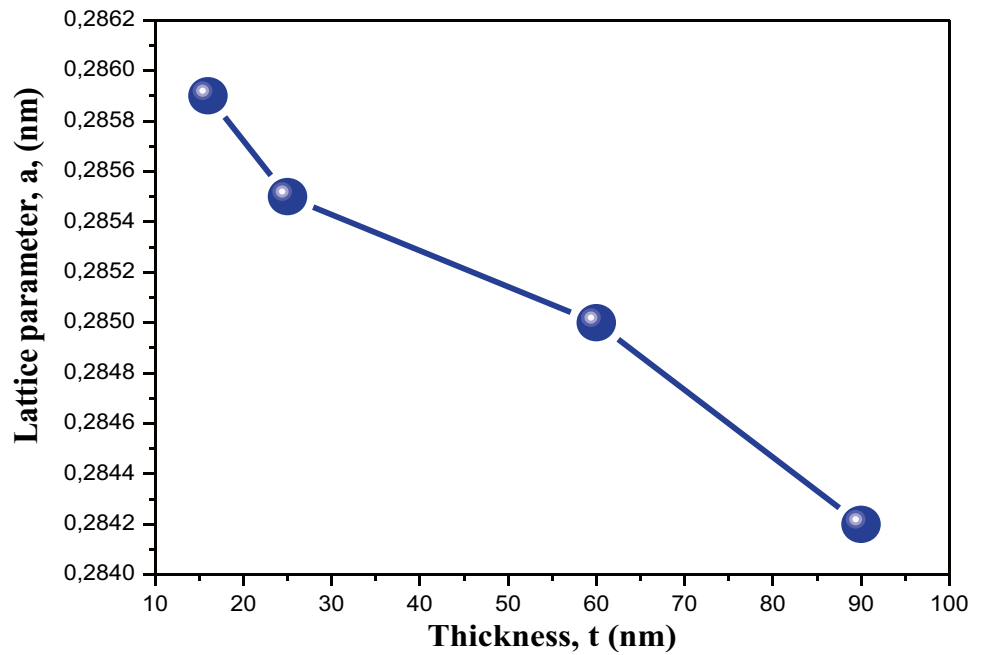
undergo structural modifications or distortions compared to their bulk counterpart. This deviation could arise from factors like surface effects, interface interactions, or other size-dependent phenomena.

The size of the mean crystallite $\langle D \rangle$ is expressed as:

$$\langle D \rangle = K \frac{\lambda}{\beta_L \cos\theta} \tag{1}$$

The integral width of the Lorentzian component, denoted as β_L , is utilized, with λ representing the wavelength of the

Fig. 6 Variations in the lattice parameter, denoted as a (nm), with changes in the thickness of $\text{Fe}_{90}\text{Sb}_{10}$ films



radiation employed. In the course of Rietveld refinement, the parameter subject to adjustment is $\langle D \rangle$.

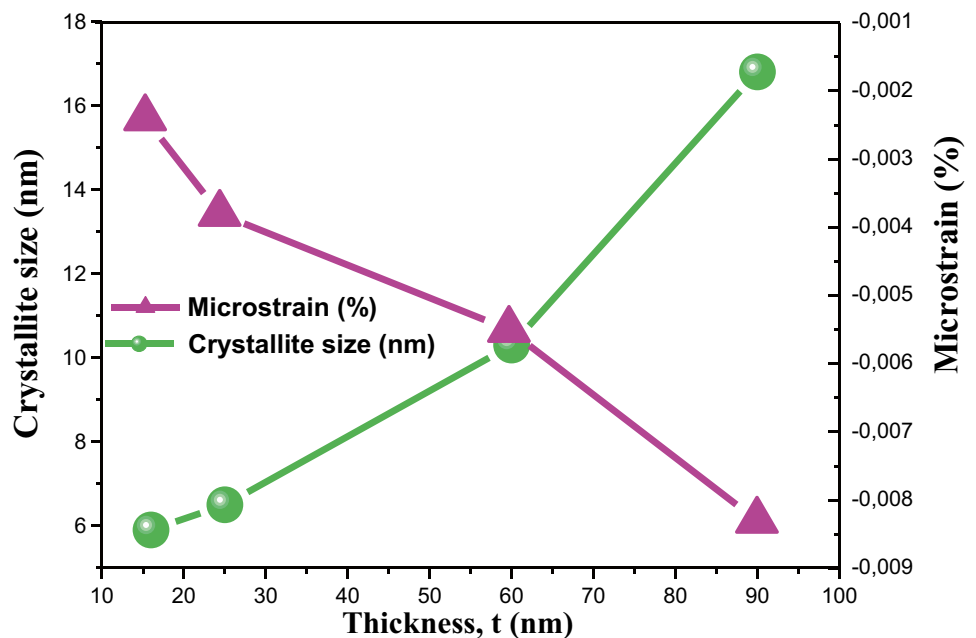
The difference between the value of the lattice parameter measured by X-ray diffraction and the value of the $\text{Fe}_{90}\text{Sb}_{10}$ bulk material gives us the microstrains ε (%):

$$\varepsilon = \frac{a_{\text{measured}} - a_{\text{bulk}}}{a_{\text{bulk}}} \quad (2)$$

Figure 7 displays evolution of average crystallite size, $\langle D \rangle$ (nm), and microstrain ε (%) of $\text{Fe}_{90}\text{Sb}_{10}$ films obtained by evaporation on glass substrates of different thicknesses 16 nm, 25 nm, 60 nm, and 90 nm. From Fig. 7, one can see that $\langle D \rangle$ increases from 5.9 to 16.8 nm, and the microstrain decreases from -0.0024 to -0.0083% with the increase of thicknesses.

The observed increase in $\langle D \rangle$ as the thicknesses increase suggests a trend of grain growth. This phenomenon is commonly associated with the coarsening of crystalline domains

Fig. 7 Evolution of the average crystallite size, $\langle D \rangle$ (nm), and microstrain ε (%) of $\text{Fe}_{90}\text{Sb}_{10}$ films versus thickness



as the material undergoes structural changes. The specific values provide quantitative insight into the scale of the crystalline structures, indicating a notable variation in the size of the crystallites with changes in thickness.

Moreover, the discernible decrease in microstrains with the augmentation of thickness implies a concurrent reduction in internal structural distortions. This phenomenon is likely attributed to the relaxation of the crystalline structure or a diminution in defects as the film thickness undergoes an increase. The negative values of microstrains signify compressive strain, indicating that the crystalline structure may be subjected to compressive effects. This intricate interplay between the mean crystallite size, microstrains, and film thickness not only underscores the structural evolution within the material but also offers nuanced insights into the dynamic processes influencing its crystalline integrity. As thickness varies, the reciprocal changes in crystallite dimensions and internal strains elucidate the intricate adjustments occurring at the atomic and microstructural levels, contributing to a comprehensive comprehension of the material's behavior under varying thickness conditions.

Figure 8 displays SEM surface images depicting variations in thickness for $\text{Fe}_{90}\text{Sb}_{10}/\text{glass}$. For the image in Fig. 8a corresponding to a $\text{Fe}_{90}\text{Sb}_{10}/\text{glass}$ film with a thickness of 16 nm, a clear depiction of a consistently even surface is observed. Not much can be discerned due to the small grain size of this sample, which is $D = 5.9$ nm, while for the thickness films 25 and 60 nm, small rounded shape droplets appear on the surface, as illustrated in Fig. 8a and b. This suggests a change in the surface morphology as the film thickness increases. In the case of the thickest film, with a

thickness of 90 nm, Fig. 8d displays a notable increase in the number of smaller rounded droplets scattered across the surface. This observation indicates a substantial alteration in the surface characteristics as the film thickness increases.

The process of fabricating $\text{Fe}_{90}\text{Sb}_{10}/\text{glass}$ films involves a crucial phase where Fe (Sb) solid solution powder undergoes a remarkable transformation. During the evaporation of iron powder, a transition from the solid to the liquid state occurs, generating a liquid phase of the material. This pivotal moment is followed by a fascinating phenomenon known as the “jet of droplets.” In this step, droplets of the liquid material, resulting from the evaporation of Fe (Sb) solid solution powder, are propelled towards the substrate with kinetic energy. The substrate, which may consist of glass in our study, plays a crucial role in the process. Upon contacting the substrate, the droplets undergo a nearly instantaneous process of cooling and solidification. This rapid cooling leads to the formation of small circular grains, also known as “droplets,” on the substrate's surface. These grains exhibit distinct morphology, influenced by the speed of the droplet jet, temperature, and other processing parameters. Thus, the phenomenon of circular grains is the result of a complex sequence of evaporation, transformation into the liquid phase, droplet projection, and finally, rapid cooling upon contact with the substrate. These observations, illustrated in the SEM images in Fig. 8, provide valuable insights into the dynamic processes during the fabrication of $\text{Fe}_{90}\text{Sb}_{10}/\text{glass}$ films at different thicknesses.

Figure 9 displays the hysteresis loops for (bcc) $\alpha\text{-Fe}$ (Sb) films on glass with varying thicknesses, measured at room temperature. These curves were acquired in the parallel

Fig. 8 SEM images of $\text{Fe}_{90}\text{Sb}_{10}/\text{glass}$ for thicknesses of **a** 16 nm, **b** 25 nm, **c** 60 nm, and **d** 90 nm

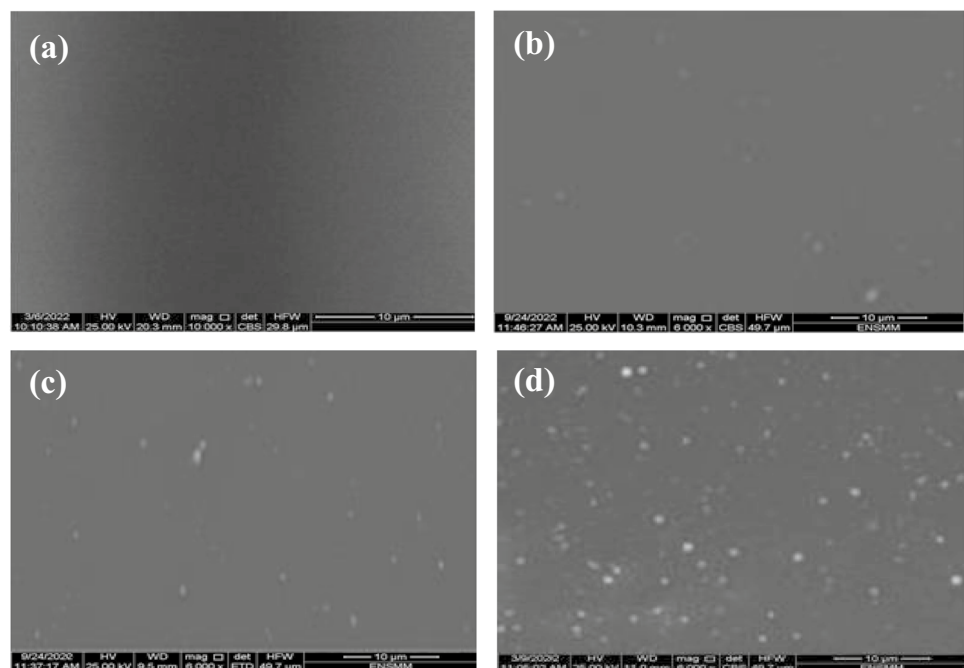
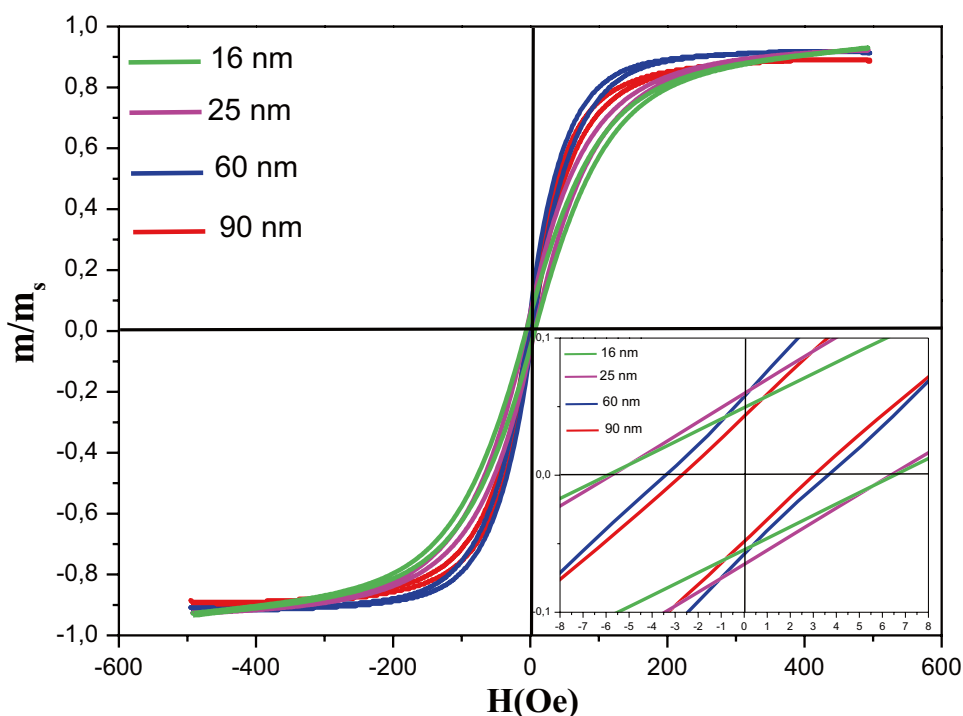


Fig. 9 Hysteresis loops for α -Fe (Sb) on glass with various thicknesses: 16 nm, 25 nm, 60 nm, and 90 nm



configuration, with the magnetic field (H) aligned in the film plane. It is found that all the cycles are saturated and have a sigmoidal shape. The low hysteresis loss observed in the cycling of the material between $-H$ and $+H$ is indicative of the efficient energy retention within the system. This phenomenon is closely linked to the soft magnetic characteristics exhibited by the layer. Soft magnetic materials are known for their ability to undergo rapid and reversible magnetization changes with minimal energy dissipation. In the context of the discussed layer, this property contributes to the overall efficiency of the material in terms of energy consumption during the cycling process. The soft magnetic nature allows the material to easily realign its magnetic domains in response to changing external magnetic fields, thereby minimizing the energy losses associated with hysteresis. This property is particularly advantageous in applications where energy efficiency and precise control of magnetic behavior are critical factors.

In Fig. 10, we present a plot of the coercive field (H_C) as a function of thickness, with H_C values ranging from 3.05 to 6.64 Oe. The observed behavior illustrates a decreasing trend in coercive field, ranging from 3.05 to 6.64 Oe, as the thickness increases from 16 to 90 nm.

The observed phenomenon in Fig. 10, where the coercive field (H_C) decreases from 3.05 to 6.64 Oe as the thickness increases from 16 to 90 nm, can be explained by the influence of thickness on the magnetic properties of the material. Coercive field is a measure of the resistance of a material to changes in its magnetization state, particularly in the context of magnetic hysteresis loops.

In this case, the decreasing trend in coercive field with increasing thickness suggests that thicker layers of the material exhibit a reduced resistance to changes in magnetization. One possible explanation for this behavior is that as the thickness of the material increases, there may be a greater volume for magnetic domains to realign or respond to an external magnetic field. This increased volume allows for a more gradual and easier realignment of the magnetic domains, leading to a lower coercive field.

The squareness S is a measure defined as the ratio of the remnant magnetization to the saturation magnetization, expressed as $S = M_r/M_s$. This parameter provides valuable insights into the magnetic behavior of thin films as a function of their thickness. The variation of the squareness S with film thickness is depicted in Fig. 11. It was observed that this ratio exhibits an intriguing trend when varying the deposition thickness. Specifically, between thicknesses of 16 nm and 25 nm, a significant increase in S was recorded. This increase can be attributed to several factors, such as size and surface effects, as well as specific interfacial interactions. At this scale, surface constraints and interfacial interactions can induce magnetic anisotropy favorable to higher remanent magnetization compared to saturation magnetization. However, beyond the thickness of 25 nm up to 90 nm, a gradual decrease in S was observed. This decrease can be explained by the increasing dominance of magneto-static effects as the deposition thickness increases. Magneto-static interactions can lead to magnetization saturation, thereby reducing the S ratio compared to smaller thicknesses.

Fig. 10 Coercive field as a function of thickness for α -Fe (Sb) deposited on glass

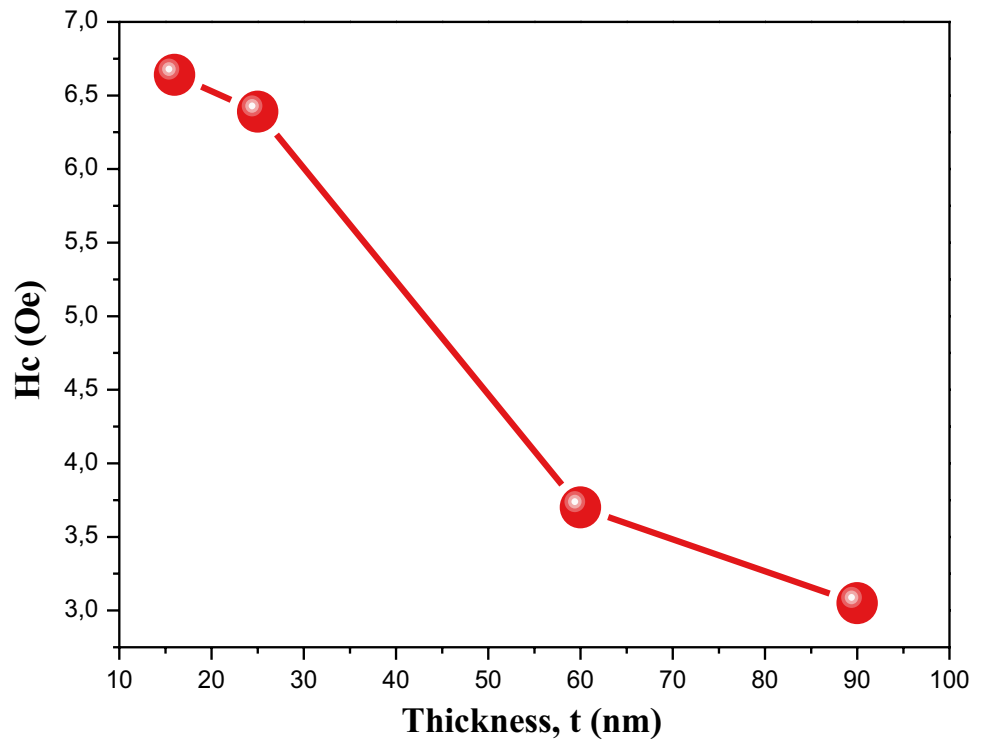
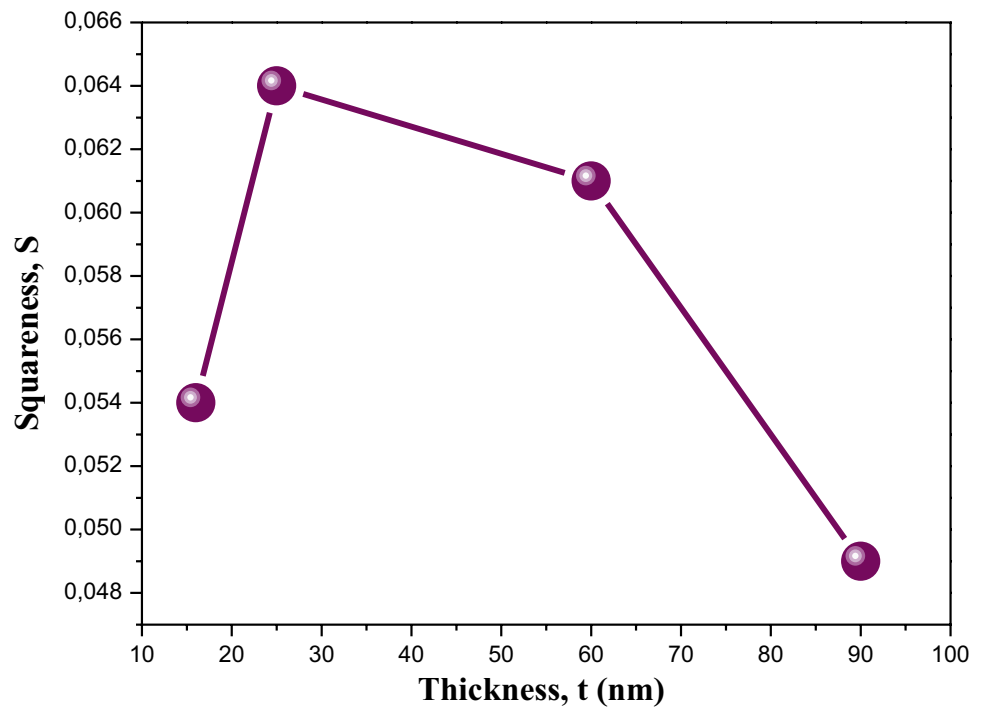


Fig. 11 The evolution of the squareness as a function of thickness for α -Fe (Sb) deposited on glass



This observation underscores the importance of considering not only the deposition thickness but also the interactions and phenomena specific to the nanoscale when designing and optimizing magnetic materials for various applications. Understanding the underlying

mechanisms of this variation in S is crucial for developing materials with optimal and predictable magnetic properties, thus paving the way for new advancements in the fields of electronics, spintronics, and magnetic device technology.

4 Conclusions

The synthesis of thin films composed of the (bcc) α -Fe(Sb) solid solution involved depositing powder that had undergone 25 h of grinding onto glass substrates using a thermal evaporation technique under vacuum conditions. Notably, all the films examined in the study exhibited tensile stress, indicating a stretching phenomenon within the material. This observation was further supported by the lattice parameter, which was slightly greater than that of the bulk material, suggesting deformation in the crystal lattice.

Analysis of the crystallite size within the films revealed variations ranging from 15 to 42 nm. These findings imply the presence of a predominantly monocrystalline structure in the films, with subtle variations in grain size across different thicknesses. As the thickness of the films increased from 16 to 90 nm, a corresponding decrease in the coercive field (H_C) was observed, ranging from 3.05 to 6.64 Oe. This decrease in H_C indicates reduced resistance to changes in magnetization, suggesting that thicker layers offer a larger volume for magnetic domains to realign. Consequently, thicker films exhibit a more gradual response to external magnetic fields, highlighting the influence of film thickness on the magnetic properties of the (bcc) α -Fe(Sb) solid solution thin films.

Acknowledgements The authors warmly thank the members of group L3M-Annaba, Dr. S. Leboub, M. Mittri, and H. Zedouri, for taking SEM pictures. This work was supported by Algerian Directorate for Scientific Research and Technological Development (DGRSDT).

Author contribution AH: synthesis and characterizations, validation, investigation, resources, writing—original draft, writing—review and editing, visualization. TH: conception, methodology, resources, review and editing, visualization, supervision, validation. DB: XRD measurements and data base, interpretation of results, manuscript preparation, visualization. AB: validation, writing—review and editing, visualization. NH: XRD refinement, visualization.

Data availability All data generated or analyzed during this study are included in this published article.

Declarations

Conflict of interest The authors declare no competing interests.

References

- Kang I, Yang J, Lee W, Seo EY, Lee DH (2023) Delineating development trends of nanotechnology in the semiconductor industry: focusing on the relationship between science and technology by employing structural topic model. *Technol Soc* 74:102326. <https://doi.org/10.1016/j.techsoc.2023.102326>
- Schummer J (2004) Multidisciplinarity, interdisciplinarity, and patterns of research collaboration in nanoscience and nanotechnology. *Scientometrics* 59(3):425–465. <https://doi.org/10.1023/B:SCIE.0000018542.71314.38>
- Islam N, Miyazaki K (2009) Nanotechnology innovation system: understanding hidden dynamics of nanoscience fusion trajectories. *Technol Forecast Soc Chang* 76(1):128–140. <https://doi.org/10.1016/j.techfore.2008.03.021>
- Wang AP, Hou CE, Hung SW (2018) Exploration of the evolution of nanotechnology from a patent co-classification perspective. *Nanotechnol* 7(3):233–245. <https://doi.org/10.1515/ntrev-2018-0005>
- Zhanga YH, Wuc LR, Maa J, Cui G (2023) Nanotechnology in solid state batteries, what's next? *Next Nanotechnol* 2:100011. <https://doi.org/10.1016/j.nxnano.2023.100011>
- Pan F, Song C, Liu XJ, Yang YC, Zeng F (2008) Ferromagnetism and possible application in spintronics of transition-metal-doped ZnO films. *Mater Sci Eng R* 62:1–35. <https://doi.org/10.1016/j.mser.2008.04.002>
- Ramasubramanian S, Thangavel R, Rajagopalan M, Thamizhavel A, Asokan K, Kanjilal D, Kumar J (2013) Study on the ferromagnetism in Co and N doped ZnO thin films. *Curr Appl Phys* 13:1547–1553. <https://doi.org/10.1016/j.cap.2013.05.010>
- Hoffmann W, Pellkofer T (2012) Thin films in photovoltaics: technologies and perspectives. *Thin Solid Films* 520(12):4094–4100. <https://doi.org/10.1016/j.tsf.2011.04.146>
- Chatzisisideris MD, Espinosa N, Laurent A, Krebs F (2016) Ecodesign perspectives of thin-film photovoltaic technologies: a review of life cycle assessment studies. *Sol Energy Mater Sol Cells* 156:2–10. <https://doi.org/10.1016/j.solmat.2016.05.048>
- Yoonho A, Jong YS (2022) Ferromagnetic properties of conducting filament nanodots formed on epitaxial BiFeO₃ thin film. *J Mater Res Technol* 18:2232–2239. <https://doi.org/10.1016/j.jmrt.2022.03.114>
- Ghebouli B, Layadi A, Kerkache L (1998) Effect of the substrate on the structural and electrical properties of dc sputtered Ni thin films. *Eur Phys J AP* 3:35–39. <https://doi.org/10.1051/epjap:1998201>
- Szmaja W, Balcerski J, Kozłowski W, Cichomski M, Grobelny J, Smolny M, Kowalczyk PJ (2012) Study of thermally evaporated thin permalloy films by the Fresnel mode of TEM and AFM. *J Alloys Compd* 521:174–177. <https://doi.org/10.1016/j.jallcom.2012.01.114>
- Wang S, Gao T, Wang C, He J (2013) Studies of anisotropic magnetoresistance and magnetic property of Ni₈₁Fe₁₉ ultra-thin films with the lower base vacuum. *J Alloys Compd* 554:405–407. <https://doi.org/10.1016/j.jallcom.2012.12.004>
- Choi JG, Hwang DG, Rhee JR, Lee SS (2010) Comparison of the soft magnetic properties of permalloy and conetic thin films. *J Magn Magn Mater* 322:2191–2194. <https://doi.org/10.1016/j.jmmm.2010.02.008>
- Hea Y, Fanc C, Lee ST (2010) Functionalisation of nanoparticles for biomedical applications. *Nano Today* 5(3):213–230. <https://doi.org/10.1016/j.nantod.2010.05.003>
- Lutterotti L (2000) Laboratorio Scienza e Tecnologia dei Materiali. Università di Torino. CORSE
- Branger V, Briand E, Kusmeruck C, Morin N, Corot F, Auburtin Ph (2002) Détermination des contraintes résiduelles par diffraction des rayons X dans des alliages d'aluminium utilisés dans l'industrie automobile. *J Phys IV France* 12(6):165–176. <https://doi.org/10.1051/jp4:20020224>
- Boukherroub N, Guittoum A, Souami N, Akkouche K, Boutarfaia S (2012) Structural, microstructural and Mössbauer studies of nanocrystalline Fe_{100-x}Al_x powders elaborated by mechanical alloying. *EPJ Web Conf* 29:00010. <https://doi.org/10.1051/epjconf/20122900010>
- Guemmod N, Hafs A, Hafs T (2022) Effect of milling time on the structural, microstructure, and magnetic properties of nanocrystalline Fe₉₀Sb₁₀ powders obtained by high-energy ball

- milling. *Int J Adv Manuf Technol* 122:2043–2058. <https://doi.org/10.1007/s00170-022-10003-x>
20. Davis RM, Dermont BM, Koch CC (1988) Mechanical alloying of brittle materials. *Met Trans A* 19:2867–2874. <https://doi.org/10.1007/BF02647712>
 21. Hasnaouia N, Hafs A, Hafs T, Bendjedaa F (2022) Structural, microstructural characterisation and magnetic properties of nanocrystalline Fe-10 wt% Pb alloy powders synthesised by mechanical alloying process. *J Alloys Compd* 899:163338. <https://doi.org/10.1016/j.jallcom.2021.163338>
 22. Yeh T, Sivertsen JM, Judy JH (1987) Thickness dependence of the magnetoresistance effect in RF sputtered thin permalloy films. *IEEE Trans Magn* 23:2215–2217. <https://doi.org/10.1109/TMAG.2018.2874169>
 23. Lamrani S, Guittoum A, Schafer R, Pofahl S, Neu V, Hemmous M, Benbrahim N (2016) Microstructure investigation and magnetic study of permalloy thin films grown by thermal evaporation. *Eur Phys J Appl Phys* 74(3):30302. <https://doi.org/10.1051/epjap/201615054>

Publisher's Note Springer Nature remains neutral with regard to jurisdictional claims in published maps and institutional affiliations.

Springer Nature or its licensor (e.g. a society or other partner) holds exclusive rights to this article under a publishing agreement with the author(s) or other rightsholder(s); author self-archiving of the accepted manuscript version of this article is solely governed by the terms of such publishing agreement and applicable law.